Paleoceanography and Paleoclimatology

RESEARCH ARTICLE
10.1029/2020PA004018

Delays, Discrepancies, and Distortions: Size-Dependent Sediment Mixing and the Deep-Sea Record of the Paleocene-Eocene Thermal Maximum From ODP Site 690 (Weddell Sea)

Brittany Hupp[1] and **D. Clay Kelly**[1]

[1]Department of Geoscience, University of Wisconsin-Madison, Madison, WI, USA

Abstract The deep-sea sedimentary record of Ocean Drilling Program Site 690 (Weddell Sea) has figured prominently in the study of an ancient (~56 Ma) global warming event referred to as the Paleocene-Eocene Thermal Maximum (PETM). Yet discrepancies in the timing, amplitude, and structure of the isotopic excursions marking the PETM exist between the bulk-carbonate and planktic foraminifer stable isotope (δ^{13}C and δ^{18}O) records of this reference section. A recent study invoked size-dependent sediment mixing (SDSM) to reconcile the discrepancies between these parallel δ^{13}C records. Here we report supplementary stable isotope data compiled from size-segregated planktic foraminifer shells that further elucidate the effects of SDSM on the Site 690 PETM section. Our records reveal a stratigraphic sequence where the carbon (CIE) and oxygen (OIE) isotope excursions marking the onset of PETM conditions are first registered by larger shells, confirming that smaller-sized pre-CIE shells have been more intensely mixed and preferentially displaced up-section into the overlying CIE interval. The size-dependent manner in which the CIE and OIE are recorded by asymbiotic subbotinids indicates that the transitory loss of size-dependent δ^{13}C signatures in photosymbiotic taxa (acarininids) at Site 690 is an artifact of SDSM. Synthetic bulk-carbonate δ^{13}C records generated with two end-member (pre-CIE versus CIE materials) sediment-mixing curves readily reproduce the series of “steps” seen in published bulk-carbonate δ^{13}C records of the CIE, suggesting that these fine-scale features may also be artifacts of SDSM and varying rates of carbonate sedimentation.

Key Points:

- Size-dependent sediment mixing accounts for multiple vagaries in stable isotope records of the iconic PETM section from ODP Site 690
- The Site 690 bulk-carbonate record has been smoothed and distorted by preferential reworking of fine-fraction carbonate
- Temporary loss of the δ^{13}C-size signature of photosymbiosis is an artifact of size-dependent sediment mixing, not a paleoecological signal

Correspondence to:
B. Hupp,
bhupp@wisc.edu

Citation:
Hupp, B., & Kelly, D. C. (2020). Delays, discrepancies, and distortions: Size-dependent sediment mixing and the deep-sea record of the Paleocene-Eocene Thermal Maximum from ODP Site 690 (Weddell Sea). *Paleoceanography and Paleoclimatology*, *35*, e2020PA004018. https://doi.org/10.1029/2020PA004018

Received 19 JUN 2020
Accepted 21 OCT 2020
Accepted article online 29 OCT 2020

1. Introduction

The carbon isotope excursion (CIE) signaling a major perturbation to global carbon cycling and the oxygen isotope excursion (OIE) reflecting ocean-climate change during an ancient (ca. 56 Ma) global warming event referred to as the Paleocene-Eocene Thermal Maximum (PETM) were first documented (Kennett & Stott, 1991) in the deep-sea sedimentary record recovered at Ocean Drilling Program (ODP) Site 690 (Figure 1). As a result, the Site 690 PETM section has garnered much attention from the scientific community, and high-resolution stable isotope (δ^{13}C and δ^{18}O) records have been constructed for this PETM section using bulk-carbonate samples (Bains et al., 1999) and planktic foraminifer shells (Thomas et al., 2002). These stable isotope records have played an important role in shaping our perception of the PETM, yet discrepancies in the timing, amplitude, and fine-scale structure of the isotopic excursions emerge when one compares the bulk-carbonate ($\delta^{13}C_{bulk}$ and $\delta^{18}O_{bulk}$) and planktic foraminifer ($\delta^{13}C_{pf}$ and $\delta^{18}O_{pf}$) records (Figure 2). Specifically, the CIE/OIE onset in the $\delta^{13}C_{pf}$ and $\delta^{18}O_{pf}$ records constructed with shells of the shallow-dwelling (euphotic zone) genus, *Acarinina*, occurs ~14 cm below where these same isotopic excursions initiate in the $\delta^{13}C_{bulk}$ and $\delta^{18}O_{bulk}$ records of the Site 690 stratigraphy (Figures 2b and 2c). Furthermore, the amplitudes of the isotopic excursions in the $\delta^{13}C_{bulk}$ and $\delta^{18}O_{bulk}$ records are appreciably smaller than those in the $\delta^{13}C_{pf}$ and $\delta^{18}O_{pf}$ records (Figures 2b and 2c), and the CIE registered in the $\delta^{13}C_{bulk}$ record shows a distinctive stepwise pattern comprising three smaller excursions that is not seen in the parallel $\delta^{13}C_{pf}$ records (Figures 2a and 2b).

In an effort to reconcile the differences between the Site 690 $\delta^{13}C_{bulk}$ and $\delta^{13}C_{pf}$ records, Hupp et al. (2019) reported δ^{13}C records compiled from graduated series of size-segregated planktic foraminifer shells straddling the pre-CIE to CIE transition and concluded that size-dependent sediment mixing (SDSM) is the

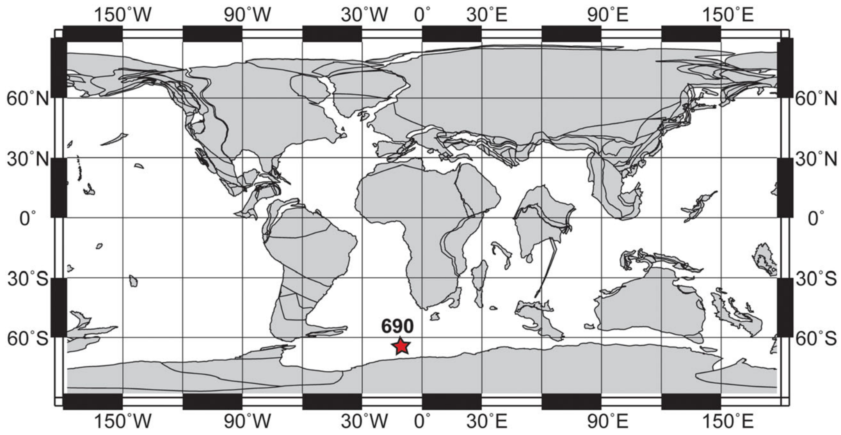

Figure 1. Paleogeographic map showing late Paleocene continental configuration and location of ODP Site 690 (red star). Base map from Ocean Drilling Stratigraphic Network (http://www.odsn.de).

principal cause of the disparities. Here, we build upon the findings of this earlier study by presenting complementary, size-segregated $\delta^{18}O_{pf}$ records for the Site 690 PETM section. We also use two end-member mixing curves to generate synthetic $\delta^{13}C_{bulk}$ records that reproduce the stepped structure of the CIE in published $\delta^{13}C_{bulk}$ records. In addition, we expand the original data set by reporting $\delta^{13}C$ and $\delta^{18}O$ records for size-segregated shells of the deep-dwelling (thermocline) planktic foraminifer genus, *Subbotina*. Inclusion of the subbotinid data permits the direct comparison of parallel, size-segregated $\delta^{13}C_{pf}$ and $\delta^{18}O_{pf}$ records constructed for both shallow dwelling (oceanic mixed layer), photosymbiont-bearing planktic foraminifers (*Acarinina*) and deep-dwelling, asymbiotic taxa (*Subbotina*). In short, we present multiple lines of evidence that point to SDSM as the singular cause of numerous disparities seen between the bulk-carbonate and planktic foraminifer stable isotope records published for the reference PETM section from Site 690.

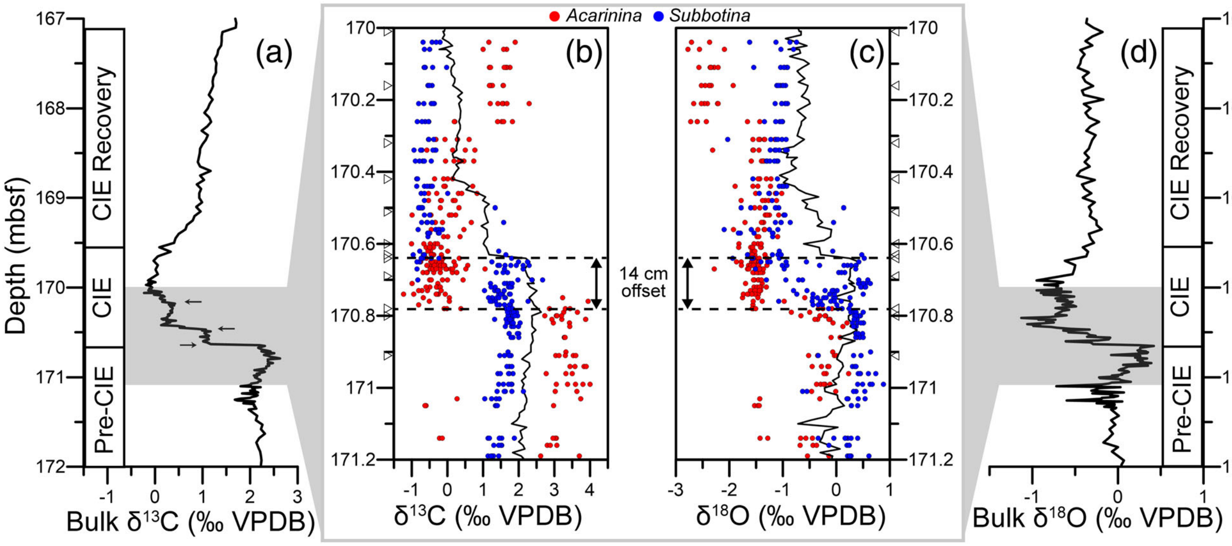

Figure 2. Bulk-carbonate (Bains et al., 1999) and planktic foraminifer (Thomas et al., 2002) stable isotope records for Site 690 PETM section. (a) Bulk-carbonate carbon isotope record showing stepped structured (arrows) of CIE. (b) Planktic foraminifer carbon isotope records of CIE overlain on bulk-carbonate carbon isotope curve (black line). (c) Planktic foraminifer records of OIE overlain on bulk-carbonate oxygen isotope curve (black line). Red and blue circles in panels (b) and (c) denote values for individual shells of the genera *Acarinina* and *Subbotina*, respectively. Note the 14-cm offset between CIE/OIE onset in *Acarinina* and bulk-carbonate records. Open triangles in panels (b) and (c) denote the stratigraphic positions of study samples. (d) Bulk-carbonate oxygen isotope record of OIE. Stratigraphic extent of study section delimited by gray shading in panels (a) and (d).

2. Materials and Methods

Site 690 is located offshore of Antarctica (65°9.63′S, 1°12.27′E) along the southwestern flank of the Maud Rise in the Weddell Sea (Figure 1) at a water depth of 2,914 m (Barker et al., 1988). Paleo-water depth estimates derived from benthic foraminifer assemblages place it within lower bathyal to upper abyssal waters (~2,000 m) during the late Paleocene (Thomas, 1990). The study section (170.01–170.91 m below seafloor, mbsf) comprises 12 core samples straddling the CIE/OIE onset (Figures 2b and 2c). The samples were disaggregated using a pH-buffered sodium hexametaphosphate hydrogen peroxide ($30\%_v$) solution, wet sieved (>63 μm), rinsed with distilled water, and oven-dried (30°C) overnight. Graduated series of size-segregated shells of the planktic foraminifer taxa *Acarinina subsphaerica*, *Acarinina soldadoensis*, and *Subbotina* spp. were handpicked from the following sieve-size fractions of each sample: 150–180 μm ($n = 16$–22), 180–212 μm ($n = 12$–16), 212–250 μm ($n = 5$–10), 250–300 μm ($n = 2$–4), and, whenever present, 300–355 μm ($n = 1$–6) and >355 μm ($n = 1$–4). The acarininid species were selected because their stable isotope signatures indicate a relatively shallow depth ecology (euphotic zone) within the oceanic mixed layer and positive covariation between their $\delta^{13}C$ signals and shell size ($\delta^{13}C$-size) suggests they hosted photosymbionts (D'Hondt et al., 1994; Norris, 1996; Quillévéré et al., 2001). Conversely, the stable isotope signatures of species belonging to the genus *Subbotina* spp. indicate a deeper depth ecology (thermocline), and the absence of $\delta^{13}C$-size covariation suggests they were asymbiotic (Norris, 1996). All planktic foraminifer shells appear opaque (frosty) under reflected light, exhibiting signs of minor to moderate degrees of diagenesis (Kozdon et al., 2020).

Stable isotope analyses were carried out on individual shells from the larger sieve-size fractions (300–355 μm and >355 μm) and then averaged for a given sample, whereas multiple shells from each of the smaller sieve-size fractions (<300 μm) were pooled for analysis. The $\delta^{13}C$ and $\delta^{18}O$ records for the two largest size fractions (300–355 μm and >355 μm) are not entirely continuous through the study section owing to an absence of larger shells in some samples. Similarly, shells for *A. soldadoensis* were extremely rare to absent in our set of pre-CIE samples. Stable isotope measurements were performed at the University of California–Santa Cruz Stable Isotope Laboratory using a ThermoScientific Kiel IV carbonate device interfaced to ThermoScientific MAT 253 dual-inlet gas-source isotope ratio mass spectrometer. External analytical precision for $\delta^{13}C$ and $\delta^{18}O$ measurements on this instrument, as determined by replicate analyses of the calcite standard Carrera Marble, was $\leq 0.1‰$ (± 2 SD). All $\delta^{13}C$ and $\delta^{18}O$ data can be accessed via the NOAA Paleoclimatology Database.

3. Results

The stable isotope values of individual (>250 μm) foraminifer shells used to construct the high-resolution $\delta^{13}C_{pf}$ and $\delta^{18}O_{pf}$ records for the Site 690 PETM section (Thomas et al., 2002) provide nominal cutoffs for differentiating pre-CIE/pre-OIE and CIE/OIE samples. We consider size classes of acarininids (*A. subsphaerica* and *A. soldadoensis*) registering $\delta^{13}C$ values $\leq 2‰$ and $\delta^{18}O$ values $\leq -1.0‰$ to be CIE and OIE samples, respectively. For the genus *Subbotina*, size classes registering $\delta^{13}C$ values $\leq 0‰$ and $\delta^{18}O$ values $\leq -0.75‰$ are CIE and OIE samples, respectively.

3.1. Shell Size and Stratigraphic Positions of Isotopic Excursions

Size-segregated $\delta^{13}C$ and $\delta^{18}O$ records constructed for all three planktic foraminifer taxa (*A. subsphaerica*, *A. soldadoensis*, and *Subbotina* spp.) are used to examine how shell size influences the stratigraphic position (i.e., timing) of the CIE/OIE onset in the Site 690 section. Stable isotope stratigraphies of two size classes (250–300 μm and 150–180 μm) with continuous records through the study section are presented for each taxon (Figure 3). An apparent “phase lag” is observed between the size-segregated stratigraphies of each taxon, where the stable isotope stratigraphies of smaller shells are shifted up-section relative to those of larger shells. This size-dependent pattern is particularly evident in the $\delta^{13}C$ and $\delta^{18}O$ records of *A. subsphaerica* (Figures 3a and 3d) and is present but less obvious in *A. soldadoensis* (Figures 3b and 3e) due to a paucity of pre-excursion shells in our samples. In the *A. subsphaerica* records (Figures 3a and 3d), the $\delta^{13}C$ and $\delta^{18}O$ values of the smallest size class (150–180 μm) never fully converge upon the more negative values registered by the larger size class (250–300 μm); hence, the magnitudes of the isotope excursions recorded by the smallest size class ($\Delta^{13}C = -2.1‰$ and $\Delta^{18}O = -0.6‰$) are not as great as those ($\Delta^{13}C = -4.1‰$ and

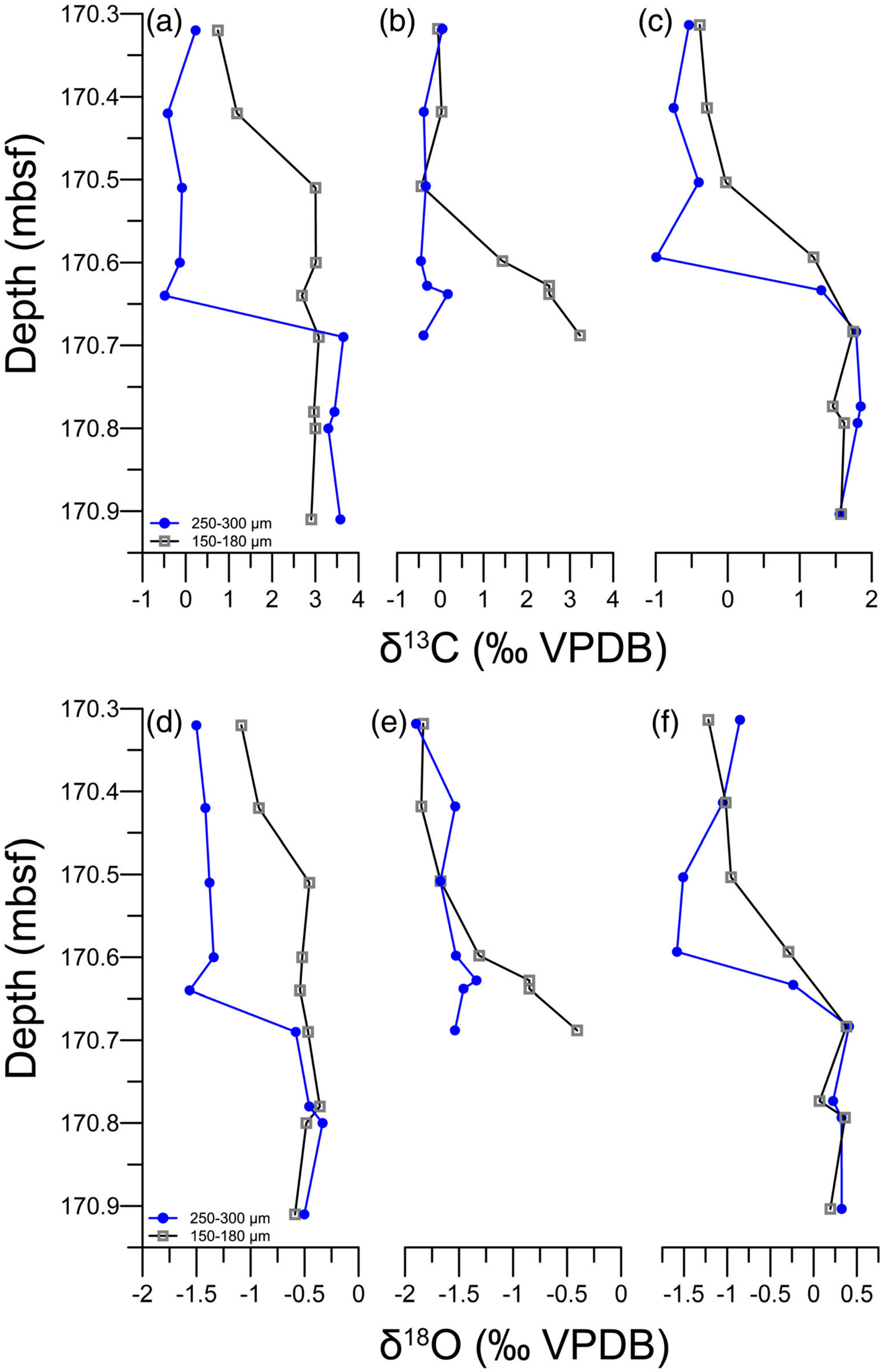

Figure 3. Comparison of planktic foraminifer carbon and oxygen isotope records constructed with large (250–300 μm, blue curves) and small (150–180 μm, gray curves) shells through the Site 690 PETM section. (a–c) Parallel carbon isotope records for (a) *Acarinina subsphaerica*, (b) *Acarinina soldadoensis*, and (c) *Subbotina* spp. (d–f) Parallel oxygen isotope records for (d) *A. subsphaerica*, (e) *A. soldadoensis*, and (f) *Subbotina* spp.

$\Delta^{18}O = -1.1‰$) registered by the larger shells (Figures 3a and 3d). A similar phase lag is observed in the size-segregated records of *Subbotina* spp., where the CIE/OIE onset is registered by the larger (250–300 μm) size class ~10 cm below where the same isotopic excursions initiate in the smallest (150–180 μm) size class (Figures 3c and 3f). Much like in the *A. subsphaerica* records, the isotopic excursions recorded by the smallest (150–180 μm) subbotinid size fraction are more gradual and somewhat muted compared to those recorded by the larger (250–300 μm) size fraction.

3.2. Stratigraphic Change in $\delta^{13}C$-Size Covariation

Stratigraphic series of samples showing secular change in the relationship between $\delta^{13}C$ values and shell sizes ($\delta^{13}C$-size) for all three planktic foraminifer taxa show how smaller shells have been preferentially displaced upward across the pre-CIE to CIE transition (Figure 4). We follow the approach used in an earlier study (Hupp et al., 2019) where the CIE onset in the $\delta^{13}C_{bulk}$ record (170.63 mbsf) is designated as a reference horizon (0 cm), with the depths of our study samples being reported relative (±cm) to this chemostratigraphic marker. Hupp et al. (2019) described the size-dependent manner in which CIE values are sequentially registered in the $\delta^{13}C$-size records of the acarininid species (*A. subsphaerica* and *A. soldadoensis*). Thus, for comparative purposes, the series of $\delta^{13}C$-size records for the acarininid species (Figures 4a–4l) is shown alongside a parallel series of $\delta^{13}C$-size records for the genus *Subbotina* spp. (Figures 4m–4r).

All size classes of *A. subsphaerica* yield pre-CIE values (~3‰ – 4‰) and delineate a $\delta^{13}C$-size trend with a positive slope in the lowermost three samples (Figure 4a). However, the $\delta^{13}C$ values of larger shells (>300 μm) abruptly decrease by ~4‰ in the overlying sample (−6 cm), while shells from the smaller size classes continue to show pre-CIE values (~3–3.5‰) and maintain the positive $\delta^{13}C$-size trend (Figure 4b). This sequential pattern of change, where each successive sample leads to the next smallest size class yielding intermediate $\delta^{13}C$ values before fully transitioning to CIE values, progresses up through the section until all *A. subsphaerica* size classes converge on ~0‰ at +47 cm (Figures 4c–4e). A pronounced $\delta^{13}C$-size relation with a positive slope is restored in the uppermost sample at +62 cm (Figure 4f).

A similar size-dependent pattern of sequential change unfolds in the $\delta^{13}C$-size relation of *A. soldadoensis* (Figures 4g–4l). The aforementioned paucity of larger (>250 μm) *A. soldadoensis* shells precluded the construction of $\delta^{13}C$-size trends for this species in the three lowermost pre-CIE samples. As a result, $\delta^{13}C$ data measured from size-segregated shells of *A. soldadoensis* from a late Paleocene (pre-CIE) sample recovered at tropical ODP Site 761 (Quillévéré et al., 2001) are shown purely for illustrative purposes (Figure 4g). Regardless, larger shells of *A. soldadoensis* return CIE values at −6 cm, while the smallest size class continues to show a pre-CIE value of ~3.2‰ (Figure 4h). Although the $\delta^{13}C$ values of the two smallest size classes remain higher than those of the larger size classes, this size-dependent pattern of change progresses up-section in the *A. soldadoensis* $\delta^{13}C$-size records until all size classes register CIE values at +3 cm (Figure 4i). In overlying samples at +12 cm and +21 cm, all size classes converge on the $\delta^{13}C$ value of ~0‰ (Figure 4j). A pronounced $\delta^{13}C$-size relation with a positive slope is reestablished in *A. soldadoensis* at the top (+62 cm) of the study section (Figure 4l).

The series of $\delta^{13}C$-size records constructed for the genus *Subbotina* also record the CIE onset in a size-dependent manner (Figures 4m–4r). Within the pre-CIE samples (Figures 4m and 4n), all size classes return $\delta^{13}C$ values (~1–2‰) characteristic of pre-CIE subbotinids and delineate little to no positive $\delta^{13}C$-size relationship. Further up-section at +3 cm, the two largest size classes return CIE values, while the smallest size class (150–180 μm) continues to show a pre-CIE value (~1.2‰), resulting in a $\delta^{13}C$-size relationship with a steep, negative slope (Figure 4o). This sequential pattern of size-dependent change culminates at +12 cm, where CIE values are registered by all the subbotinid size classes (Figure 4p). All subbotinid size classes continue to show CIE values (<0‰) with no clear $\delta^{13}C$-size trend in the overlying samples at the top of the study section (Figures 4q and 4r).

In summary, the $\delta^{13}C$-size records of all three taxa show a similar pattern of stratigraphic change, where the positive covariation recorded by pre-CIE shells temporarily shifts to a negative phase of $\delta^{13}C$-size covariation before all of the size classes register CIE values with no clear $\delta^{13}C$-size trend. The thicknesses of the stratigraphic intervals required for all size classes to transition to CIE values vary between taxa, being greater in *A. subsphaerica* (~27 cm) than in the other two taxa (~9 cm). Moreover, the core depth where the CIE onset is first recorded by larger shells is stratigraphically staggered among the three taxa, with CIE values being first

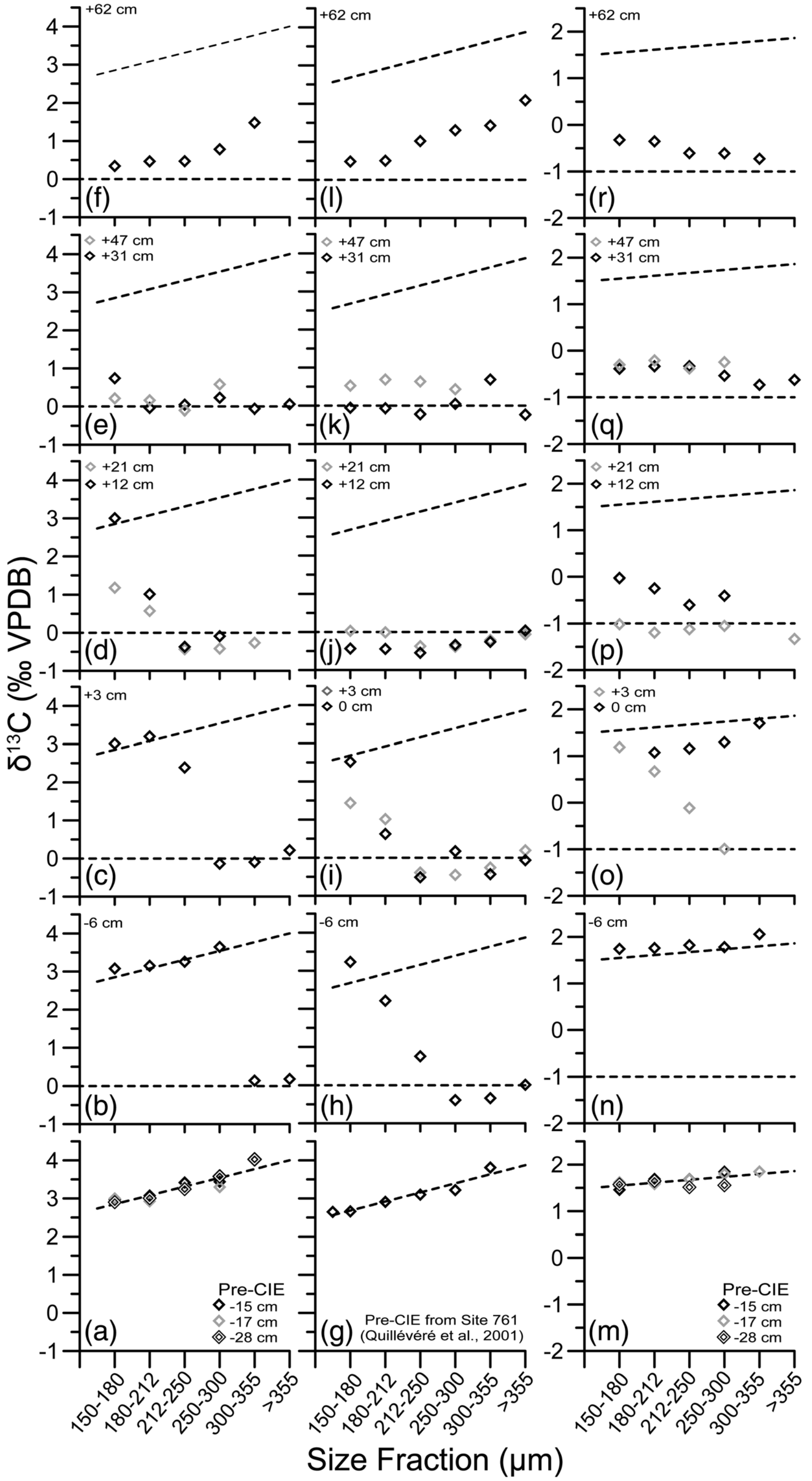

Figure 4. Stratigraphic series of size-segregated carbon isotope records for three planktic foraminifer taxa through the Site 690 PETM section. (a–f) *Acarinina subsphaerica*, (g–l) *Acarinina soldadoensis*, and (m–r) *Subbotina* spp. Dashed lines with positive slopes show pre-CIE values and trends, and horizontal dashed lines serve as visual aids and approximate fully developed CIE values. Note pre-CIE trend for *A. soldadoensis* (g) taken from the late Paleocene sample of ODP Site 761 (Quillévéré et al., 2001) is shown purely for illustrative purposes. Core depths of samples reported relative (±cm) to the stratigraphic level of CIE onset in bulk-carbonate record.

registered by larger (>250 μm) shells of both acarininid species at −6 cm (Figures 4b and 4h) and at + 3 cm in larger subbotinids (Figure 4o).

3.3. Stratigraphic Change in δ^{18}O-Size Covariation

The sequential pattern of size-dependent change seen in the δ^{13}C-size records is also expressed in the complementary δ^{18}O-size records of all three taxa (Figure 5). The onsets of the CIE and OIE occur at the same core depth in the Site 690 bulk-carbonate record; hence, the core depths of samples showing δ^{18}O-size trends are reported relative (± cm) to the OIE onset in the $\delta^{18}O_{bulk}$ stratigraphy. The δ^{18}O-size trends of *A. subsphaerica* best illustrate the size-dependent change from pre-OIE to OIE values (Figures 5a–5f). All size classes of *A. subsphaerica* return pre-OIE values centered on −0.5‰ (Figure 5a). In the overlying sample at −6 cm, the δ^{18}O of the largest size class (>355 μm) decreases to an OIE value of −1.6‰, and the next largest size class (300–355 μm) registers a transitional value of −1.0‰, while the smaller size classes continue to show pre-OIE values (Figure 5b). In the succeeding sample at + 3 cm, the three largest size classes record OIE values, whereas the 212–250 μm size fraction yields an intermediate δ^{18}O value of −0.7‰, and the two smallest size fractions continue to record pre-OIE values centered on −0.5‰ (Figure 5c). This sequential pattern of size-dependent change progresses up through the study section (Figures 5a–5e).

And while the two smallest size fractions (150–180 μm and 180–212 μm) never fully transition to OIE values in the uppermost sample (+62 cm), the largest size fraction (300–355 μm) registers the lowest value (−2.1‰) of the entire *A. subsphaerica* δ^{18}O-size series with the two next largest size fractions (250–300 μm and 212–250 μm) returning OIE values (Figure 5f). The size-dependent pattern of change in the uppermost sample (+62 cm) results in a pronounced δ^{18}O-size relationship with a negative slope (Figure 5f) that resembles the negative δ^{18}O-size relationship seen at −6 cm (Figure 5b).

A paucity of pre-OIE *A. soldadoensis* shells and the lack of suitable size-segregated δ^{18}O data from other nearby locales precluded the construction of δ^{18}O-size records for the lowermost three samples in our study section. Still, the four largest size classes of *A. soldadoensis* return OIE values at −6 cm, while the 180–212 μm size fraction registers an intermediate value (−0.7‰) and the smallest size fraction continues to show a pre-OIE value (Figure 5g). Only the smallest size class (150–180 μm) records a pre-OIE value at 0 cm, and all size classes have transitioned to OIE values by sample + 3 cm (Figure 5h). In the sample at the top of the study section (+62 cm), the four largest size classes undergo a secondary decrease where their δ^{18}O values fall just below −2.0‰, while the two smallest size classes continue to return slightly higher OIE values (Figure 5k).

The series of δ^{18}O-size records for the subbotinids (Figures 5l–5q) show a sequential pattern of size-dependent change similar to that seen in the acarininid species. In the three lowermost samples, all size classes of subbotinids register pre-OIE values (Figure 5l). The δ^{18}O of the largest size class (300–355 μm) decreases by ~1.0‰ and approaches an OIE value in the overlying sample at −6 cm then abruptly increases to a pre-OIE value at 0 cm before fully transitioning to an OIE value (−1.6‰) at + 3 cm (Figures 5m and 5n). By contrast, the two smallest size classes from this same stratigraphic interval register pre-OIE values (Figures 5m and 5n). Finally, all subbotinid size classes fully transition to OIE values by + 12 cm (Figure 5o) and maintain OIE values through the remainder of the overlying study section (Figures 5o–5q).

4. Discussion

A hallmark of the PETM is a global decrease in the δ^{13}C composition of both marine and terrestrial carbon-bearing materials (Bains et al., 1999; Bowen et al., 2015; Bowen & Bowen, 2008; Koch et al., 1992; McInerney & Wing, 2011). This CIE signals the rapid (≤5 kyr) influx of isotopically light carbon into Earth's surficial carbon cycle (Dickens et al., 1995; Kirtland Turner et al., 2017; Svenson et al., 2004; Zeebe et al., 2009) and is accompanied by a negative OIE in pelagic records reflecting an average warming of ~5°C across Earth's surface ocean (Aze et al., 2014; Dunkley Jones et al., 2013). Thus, the CIE represents a chemostratigraphic datum that is used for global correlation (Aubry et al., 2007).

4.1. Size-Dependent Phase Lags

The CIE and OIE marking the PETM were first documented at Site 690 (Kennett & Stott, 1991), and this record has since been treated as a type of reference section to which other PETM records are compared

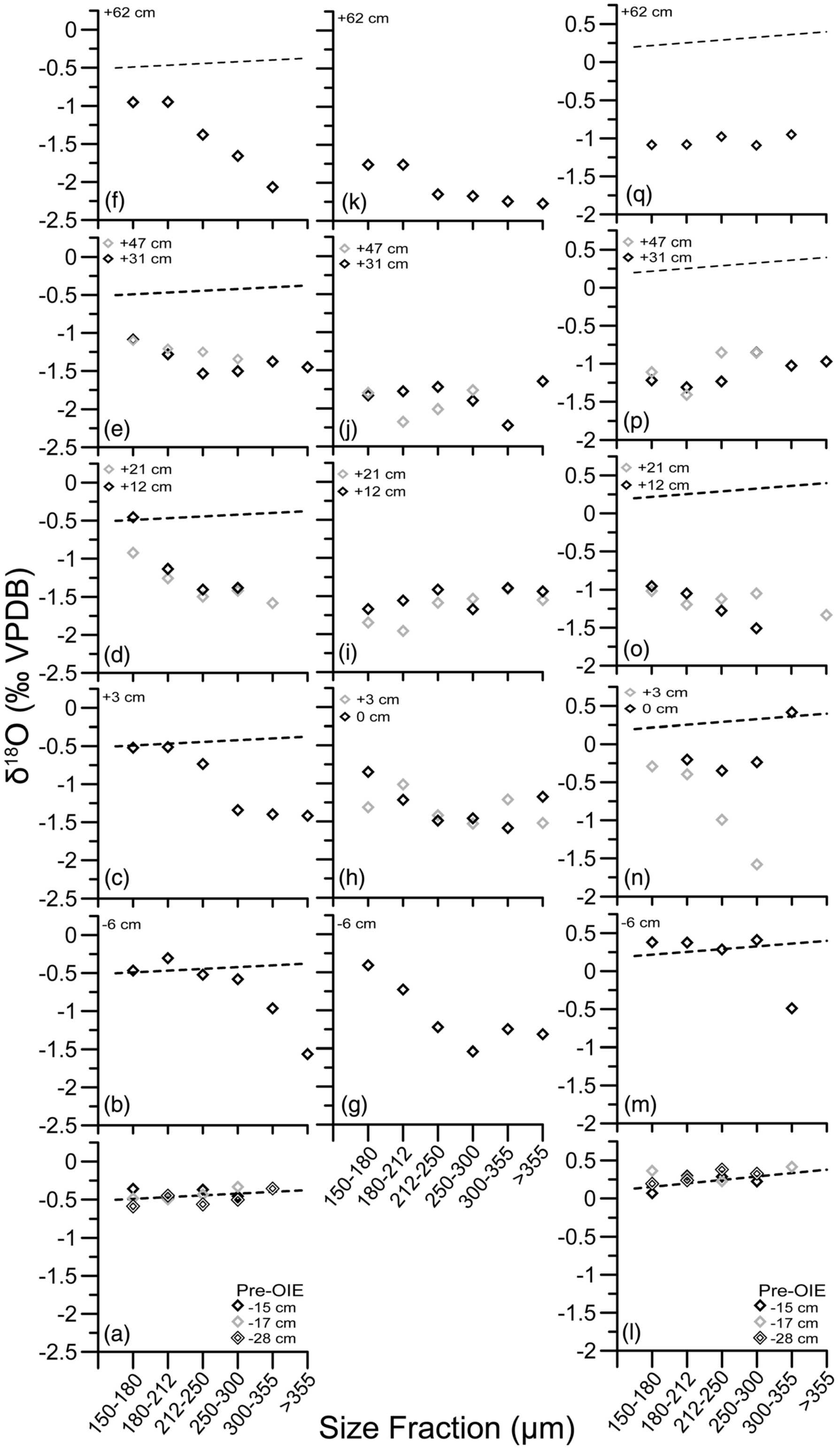

Figure 5. Stratigraphic series of size segregated oxygen isotope records for three planktic foraminifer taxa through the Site 690 PETM section. (a–f) *Acarinina subsphaerica*, (g–k) *Acarinina soldadoensis*, and (l–q) *Subbotina* spp. Dashed lines show pre-OIE values and trends. Note paucity of shells in study samples and lack of suitable data in literature precludes construction of pre-OIE δ^{18}O-size relation for *A. soldadoensis*. Core depths of samples reported relative (±cm) to the stratigraphic level of CIE onset in bulk-carbonate record.

(e.g., Bains et al., 1999; Kelly et al., 2010; Penman & Zachos, 2018; Zachos et al., 2005; Zhang et al., 2020). However, the depth of the CIE/OIE onset in the $\delta^{13}C_{bulk}$ and $\delta^{18}O_{bulk}$ records is ~14 cm above where the onsets of these same isotopic excursions occur in the acarininid $\delta^{13}C$ and $\delta^{18}O$ records (Figures 2b and 2c). An astronomically tuned age model constructed for the Site 690 PETM section (Röhl et al., 2007) indicates that this 14-cm offset equates to a temporal phase lag of about 7.31 ka. This stratigraphic offset may seem immaterial at first blush, but pinpointing the stratigraphic level of the CIE/OIE onset is crucial to determining the relative timing of events that unfolded during the pre-CIE to CIE transition (e.g., Kozdon et al., 2020; Thomas et al., 2002).

There is now a wealth of evidence to indicate that the stratigraphy of the Site 690 PETM section has been disturbed by sediment mixing processes. Mechanisms for such sediment mixing include winnowing and redeposition by bottom-water currents (Seibold, 1978) and the burrowing activity of benthic organisms (bioturbation) (Berger & Heath, 1968; Berger & Johnson, 1978; Ridgwell, 2007; Schiffelbein, 1984). The bimodal distribution of $\delta^{13}C$ values compiled from individual foraminifer shells at, and directly above, the CIE onset (Figure 2b) shows that these microfossil assemblages are mixtures of pre-CIE shells with high $\delta^{13}C$ values and CIE shells with anomalously low $\delta^{13}C$ values (Zachos et al., 2007). Core photographs also show visible signs of bioturbation across the base of the Site 690 PETM section (Bralower et al., 2014), and sedimentological records (i.e., wt% coarse fraction) from nearby Site 689 suggest that the area has been subject to winnowing by bottom-water currents (Kelly et al., 2012). Finally, modeling studies have shown how the bulk-carbonate record and the stratigraphic distribution of individual foraminifer shells within the Site 690 PETM section may be manipulated by sediment mixing processes (Kirtland Turner et al., 2017; Ridgwell, 2007).

Additional clues as to the cause of the phase lag seen between the Site 690 bulk-carbonate and acarininid $\delta^{13}C$ records are provided by sedimentological studies. Grain-size analysis has shown that fine-grained (<10 μm) nannofossils are the chief constituent of bulk carbonate in the Site 690 PETM section (Bralower et al., 2014); thus, the bulk-carbonate records primarily reflect the isotopic composition of fine-fraction carbonate consisting of calcareous nannofossils (Bralower, 2002; Stoll, 2005). Taken at face value, the stratigraphic offset suggests a ~7 kyr delay between the responses of acarininid planktic foraminifers and calcareous nannoplankton, but such a lengthy delay is unlikely given how well-mixed dissolved inorganic carbon is within the surface ocean (euphotic zone) where both the photosymbiont-bearing acarininids and photoautotrophic nannoplankton dwelled (e.g., Kirtland Turner et al., 2017; Stoll, 2005). A diagenetic mechanism for such a stratigraphic offset seems implausible since seafloor diagenesis tends to increase the $\delta^{18}O$ of foraminifer calcite (Kozdon et al., 2013; Pearson et al., 2001), yet $\delta^{18}O$ values decrease over the CIE/OIE interval. Though the isotopic compositions of foraminifer shells within the Site 690 PETM section appear to have been altered (Kozdon et al., 2020), studies indicate that stratigraphic trends in stable isotope records signaling environmental change and secular variation in ocean chemistry are not expunged from the deep-sea sedimentary record by diagenesis (Edgar et al., 2015; Stainbank et al., 2020). Moreover, some of the smaller size classes of reworked shells within the CIE interval register $\delta^{13}C$ (~3‰) and $\delta^{18}O$ (−0.5‰) values that are remarkably similar to those of similarly sized shells within the underlying pre-CIE interval (Figures 4a–4d and 5a–5d). The planktic foraminifer $\delta^{13}C$ and $\delta^{18}O$ records herein reported show that successively smaller size classes of shells sequentially record CIE/OIE values up through the Site 690 PETM stratigraphy (Figures 3–5), which is consistent with fine-sized materials such as nannofossils being more intensely mixed than coarse-sized (>250 μm) foraminifer shells. We therefore seek a taphonomic mechanism that accounts for the differential displacement of fine-fraction carbonate and larger-sized planktic foraminifer shells.

Both model- and experimental-driven studies indicate that deposit-feeding benthic organisms preferentially ingest smaller-sized particles (Jumars et al., 1981; Taghon, 1982; Wheatcroft & Jumars, 1987) and that subsequent deposition of fecal pellets can prolong the residence time of smaller particles within the surficial mixing layer of pelagic sediments (Jumars et al., 1981). In addition, meiofaunas are an underappreciated benthic biota composed of myriad interstitial microorganisms (~50 μm to 1 mm) that preferentially displace finer-grained sediments, and the "biological winnowing" of their activity transports finer particles to the sediment surface (Murray et al., 2002). Based on the evidence at hand, the phase lag between the acarininid and nannofossil-dominated bulk carbonate records is likely an artifact of particle size-selective feeding by infauna (bioturbation), although physical winnowing of sediments by bottom-water currents need not be excluded.

The stratigraphic offset between the bulk-carbonate and planktic foraminifer records raises the following question: Which of these two records should be used to delimit the CIE/OIE onset? Statistical analysis of grain-size data from pelagic sediments indicates that larger microfossils should be used in high-resolution stratigraphic studies (Wheatcroft & Jumars, 1987). The size-dependent phase lags expressed in our $\delta^{13}C_{pf}$ and $\delta^{18}O_{pf}$ records support this view. We therefore recommend that, whenever possible, stable isotope data acquired from relatively large (>250 μm) foraminifer shells that are less susceptible to upward displacement in pelagic sediments be used to construct high-resolution CIE/OIE records.

4.2. Attenuated Amplitudes and Inverted Isotope Gradients

The amplitudes of the CIE and OIE provide constraints on respective estimates of carbon input and degree of ocean warming during the PETM (e.g., Dickens et al., 1995; Dunkley Jones et al., 2013; Kennett & Stott, 1991; McInerney & Wing, 2011). However, the amplitudes of these isotopic excursions in the bulk-carbonate records are smaller than those registered by the acarininid records at Site 690. The amplitude of the CIE in the nannofossil-dominated $\delta^{13}C_{bulk}$ record (~2.2‰) is only about half that (~4‰) registered by the acarininid $\delta^{13}C_{pf}$ record (Figure 2b). Likewise, the amplitude of the OIE in the nannofossil-dominated $\delta^{18}O_{bulk}$ record (~1‰) appears attenuated compared to that (~2‰) registered by the acarininid $\delta^{18}O_{pf}$ record (Figure 2c).

The differences between the amplitudes of these isotopic excursions are readily explained by SDSM. Sediment mixing has long been recognized as a mechanism for blending sediments on the seafloor (Bard, 2001; Berger & Johnson, 1978; Glass, 1969; Peng et al., 1979), and its time-averaging effects have been shown to smooth and attenuate paleoclimate signals preserved in pelagic records (Schiffelbein, 1984). The size-dependent nature of the phase lags seen in our $\delta^{13}C_{pf}$ and $\delta^{18}O_{pf}$ records for shallow- and thermocline-dwelling taxa indicate that finer-sized particles are more intensely mixed and preferentially displaced upward in the Site 690 stratigraphy (Figures 3–5). We posit that the finer grain size composition of nannofossil-dominated bulk-carbonate samples makes them more susceptible to upward displacement, causing their isotopic excursions to be shifted up-section and attenuated.

SDSM manifests in the Site 690 PETM section in other ways. Most notably, the combined effect of the phase lags and attenuated amplitudes results in transient inversions of the isotopic gradients between the bulk-carbonate and planktic foraminifer records. For instance, acarininid $\delta^{13}C$ values are higher than those of the nannofossil-dominated $\delta^{13}C_{bulk}$ curve within the pre-CIE interval but abruptly drop to values lower than the nannofossil-dominated $\delta^{13}C_{bulk}$ curve within the overlying CIE interval (Figure 2b). This $\delta^{13}C$ phase shift persists for ~50 cm above the stratigraphic level where the CIE onset occurs in the acarininid $\delta^{13}C$ record (170.78 mbsf) and abruptly ends at ~170.30 mbsf where $\delta^{13}C$ values of larger (>250 μm) acarininid shells increase by ~1‰. Such reversals in isotopic gradients have been attributed to changes in primary productivity and water column stratification as the PETM unfolded at Site 690 (e.g., Kennett & Stott, 1991; Stoll, 2005). However, we note that the $\delta^{13}C$ values of the smallest size class (150–180 μm) of *A. subsphaerica* do not fully transition to CIE values until ~47 cm above the CIE onset in the $\delta^{13}C_{bulk}$ record (Figures 4a–4e). This finding suggests that the deleterious effects of SDSM reach well beyond the pre-CIE to CIE transition in the Site 690 stratigraphy (Hupp et al., 2019), and we consider SDSM to be the cause of the transient inversion of the gradient between the acarininid and bulk-carbonate $\delta^{13}C$ curves.

A similar but less pronounced phase shift occurs between the subbotinid $\delta^{18}O_{pf}$ and nannofossil-dominated $\delta^{18}O_{bulk}$ records. Subbotinid $\delta^{18}O$ values are, on average, higher than those registered in the nannofossil-dominated $\delta^{18}O_{bulk}$ curve within the pre-OIE interval but decrease to values lower than the $\delta^{18}O_{bulk}$ curve across OIE onset and remain below the nannofossil-dominated $\delta^{18}O_{bulk}$ curve for the remainder of the study section (Figure 2c). Given the size-dependent nature of the OIE onset in our subbotinid $\delta^{18}O_{pf}$ records (Figure 3f), we argue that the phase shift seen between the subbotinid $\delta^{18}O_{pf}$ and $\delta^{18}O_{bulk}$ records (Figure 2c) is yet another artifact of SDSM where the negative amplitude of the OIE in the nannofossil-dominated $\delta^{18}O_{bulk}$ record has been attenuated by the upward reworking of pre-OIE fine-fraction carbonate with higher $\delta^{18}O$ values.

4.3. A Stepwise CIE: Fact or Artifact?

The CIE profiles delineated by the parallel $\delta^{13}C_{bulk}$ and $\delta^{13}C_{pf}$ stratigraphies constructed for the Site 690 PETM section differ in their fine-scale structure. Specifically, the nannofossil-dominated $\delta^{13}C_{bulk}$ stratigraphy comprises a stepwise series of three smaller isotopic decreases bounded by periods of stasis that eventually culminate in a minimum $\delta^{13}C_{bulk}$ value (−0.23‰) centered on ~170.00 mbsf (Figure 2a), whereas the CIE in the acarininid $\delta^{13}C_{pf}$ record is expressed as a single, abrupt decrease on the order of ~4‰ at 170.78 mbsf (Figure 2b). Thus, the stepped series of smaller isotopic decreases seen in the nannofossil-dominated $\delta^{13}C_{bulk}$ record is not present in the complementary acarininid $\delta^{13}C_{pf}$ record.

The series of "steps" embedded within the $\delta^{13}C_{bulk}$ record was first recognized in the Site 690 PETM section and interpreted as signaling multiple pulses of carbon input during the PETM (Bains et al., 1999). This step-like CIE structure has since been recognized in the $\delta^{13}C_{bulk}$ records of other pelagic PETM sections and used as a further means of global correlation (e.g., Bains et al., 1999; Jiang & Wise, 2009; Kelly et al., 2012; Röhl et al., 2007; Zachos et al., 2005). The stepped structure of the bulk-carbonate CIE record has been replicated in $\delta^{13}C$ records constructed with near-monogeneric concentrates of the nannofossil taxa *Chiasmolithus* and *Toweius* taken from the Site 690 PETM section; hence, the steps were thought to reflect true environmental change (Stoll, 2005). However, if the series of isotopic decreases seen in the Site 690 bulk-carbonate CIE record chronicles a stepwise change to $\delta^{13}C$ of dissolved inorganic carbon, then why is this stepped structure not expressed in the complementary acarininid $\delta^{13}C_{pf}$ record?

Here we examine multiple lines of evidence to gain insight into the mechanism(s) that may have given rise to the stepped structure of the bulk-carbonate CIE record. Census counts show that the two taxa (*Chiasmolithus* and *Toweius*) used to construct the stepped, monogeneric $\delta^{13}C$ records are the two most abundant genera in pre-CIE nannofossil assemblages and that their stratigraphic ranges extend across the CIE onset at Site 690 (Bralower, 2002). It therefore stands to reason that the steps seen in both the monogeneric nannofossil $\delta^{13}C$ and $\delta^{13}C_{bulk}$ records share a common cause, namely, SDSM, where nannofossils are preferentially displaced up-section with the proportion of reworked pre-CIE nannofossils decreasing in a discontinuous (stepped) manner through the overlying CIE interval.

As a first-order approximation of how the amount of reworked pre-CIE material might vary up through the overlying CIE interval, we constructed a series of deterministic mixing curves along which the proportions of pre-CIE and CIE carbonate are varied so that the resulting synthetic $\delta^{13}C_{bulk}$ curves match the $\delta^{13}C$ values and stepped structure of the published $\delta^{13}C_{bulk}$ record (Figure 6). Thus, the calculated proportion of pre-CIE carbonate is a function of the actual $\delta^{13}C_{bulk}$ value reported for the sample and the $\delta^{13}C_{bulk}$ values prescribed to the two mixing components. The highest value (2.5‰) from the pre-CIE interval of the published Site 690 $\delta^{13}C_{bulk}$ record was taken to represent the $\delta^{13}C_{bulk}$ end-member value of pre-CIE carbonate in all three mixing curves, whereas CIE carbonate is assigned a different $\delta^{13}C_{bulk}$ value in each of the mixing curves (Figure 6). We acknowledge that bulk-carbonate samples are amalgamations of different microfossils with disparate $\delta^{13}C$ signatures and that assigning "fixed" $\delta^{13}C_{bulk}$ values to the mixing components belies their heterogeneous compositions. Still, we feel that this simplistic approach is acceptable because the distribution of $\delta^{13}C$ values measured from individual foraminifer shells from multiple PETM sections lack intermediate values and are distinctly bimodal (Zachos et al., 2007). Thus, for the purposes of this conceptual exercise, we assume that a similar bimodality exists in the $\delta^{13}C$ distributions of all carbonate substrates within the narrow confines of the targeted study interval. All of the mixing curves initiate within the pre-CIE interval (171.20 mbsf) and extend upward to just above the stratigraphic level of the CIE minimum (169.90 mbsf) in the published $\delta^{13}C_{bulk}$ record.

The pre-CIE records of the three mixing curves show a high degree of similitude because only minor amounts (0–20%) of contamination from CIE carbonate are required to match the published $\delta^{13}C$ values (Figure 6). This result indicates that small quantities of CIE material have been displaced downward in the stratigraphy, which is consistent with the handful of CIE acarininid shells within the underlying pre-CIE interval of the Site 690 PETM section (see Figure 2b). By contrast, the proportions of pre-CIE carbonate reworked into the overlying CIE interval differ between the three mixing curves (Figure 6). These differences are a function of the $\delta^{13}C_{bulk}$ values assigned to CIE carbonate in the mixing curves; nevertheless, the computed proportions of pre-CIE carbonate loosely constrain the amounts of reworked sediment up through the CIE interval of the $\delta^{13}C_{bulk}$ record.

The first mixing curve serves as a conservative "null" hypothesis (Figure 6a), where CIE carbonate is assigned the minimum value (−0.23‰) in the published $\delta^{13}C_{bulk}$ record under the assumption that it reflects the true $\delta^{13}C_{bulk}$ composition of pure (100%) CIE carbonate. This mixing curve shows that bulk carbonate

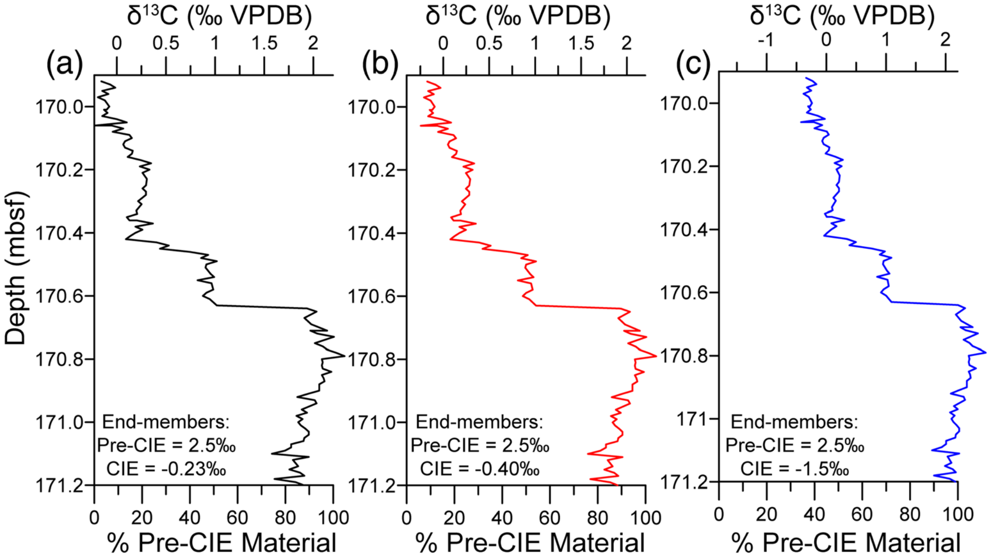

Figure 6. Synthetic bulk-carbonate carbon isotope records of the CIE generated using mixing curves based on two components (pre-CIE vs. CIE materials) with fixed bulk δ^{13}C values. The pre-CIE component is 2.5‰ in all three mixing curves. (a) CIE component is the minimum δ^{13}C value of −0.23‰ in the published bulk-carbonate record. (b) CIE component is the average planktic foraminifer CIE value of −0.40‰. (c) CIE component is −1.5‰ and assumes an excursion magnitude of 4‰. Note synthetic curves reproduce the stepped structure of published bulk-carbonate record and provide first-order estimates for the amount of pre-CIE material, namely, fine-fraction nannofossils, mixed (reworked) into overlying CIE interval.

associated with the initial isotopic decrease at 170.63 mbsf is composed of ~45% pre-CIE material. In the second mixing curve (Figure 6b), the mean $\delta^{13}C_{pf}$ value of all planktic foraminifer shells (acarininids and subbotinids) that returned CIE values (−0.40‰) is used to represent the $\delta^{13}C_{bulk}$ of CIE carbonate. This mixing curve suggests that bulk carbonate within the interval of the initial isotopic decrease consists of ~50% pre-CIE material. Finally, the $\delta^{13}C_{bulk}$ value assigned to CIE carbonate (−1.5‰) in the third mixing curve reflects a change in $\delta^{13}C_{bulk}$ commensurate with a CIE amplitude of −4‰ (Figure 6c). Owing to the lower $\delta^{13}C_{bulk}$ value assigned to CIE carbonate, an even greater amount of reworked pre-CIE carbonate (~65%) is required to reproduce the actual (published) $\delta^{13}C_{bulk}$ value of the initial isotopic decrease (Figure 6c).

All three mixing curves indicate that substantial quantities of fine-fraction carbonate from the underlying pre-CIE interval have been reworked up into the CIE interval (Figure 6). This would explain why the initial isotopic decrease (step) signaling the CIE onset in the $\delta^{13}C_{bulk}$ record is only ~1‰ compared to the ~4‰ decrease registered in the acarininid $\delta^{13}C_{pf}$ record. It also indicates that sedimentary calcite content (wt% $CaCO_3$) has been artificially elevated across the CIE onset, suggesting that carbonate dissolution was more severe at Site 690 than wt% $CaCO_3$ records indicate (Farley & Eltgroth, 2003; Kelly et al., 2005) and that the base of this reference PETM section is truncated by a hiatus (e.g., Ajayi et al., 2020; Westerhold et al., 2018; Zhang et al., 2020). In addition, studies have shown that calcareous nannofloras were profoundly perturbed by the onset of PETM conditions at Site 690 (Bralower, 2002). Yet, even our most conservative estimate for sediment mixing (Figure 6a) suggests that these nannofossil assemblages contain significant amounts (~45%) of fine-fraction carbonate reworked from the underlying pre-CIE interval; thus, the magnitude of taxonomic turnover in nannofloras at Site 690 is likely greater than perceived.

The series of mixing curves (Figure 6) also show that the stepped structure of the Site 690 $\delta^{13}C_{bulk}$ record can be reproduced by simply altering the proportions of pre-CIE and CIE material and that a lesser proportion of pre-CIE material is incorporated into the section with each step. This suggests that the steps in the $\delta^{13}C_{bulk}$ record are artifacts of discrete "jumps" in carbonate sedimentation that reduced the amount of reworked pre-CIE material incorporated into the overlying section. Rapid carbon input fueled ocean acidification and carbonate dissolution at the onset of the CIE, causing the lysocline to shoal (e.g., Babila et al., 2018; Dickens et al., 1997; Zeebe et al., 2009); however, the lysocline subsequently subsided to deeper depths as marine carbonate chemistry began to recover from the initial perturbation (Kelly et al., 2005, 2010, 2012; Penman et al., 2016; Zachos et al., 2005). Thus, we consider the series of steps in the $\delta^{13}C_{bulk}$ record to signal pulsed increases in carbonate sedimentation as the lysocline deepened. The initial rise and subsequent fall of the carbonate lysocline occurred in all of the ocean basins (Dickens et al., 1997; Zeebe et al., 2009), so the stepped structure of the CIE would likely manifest in the $\delta^{13}C_{bulk}$ records at other pelagic sites and may still be suitable for intersite correlation over broad geographic regions on millennial time scales (e.g., Bains et al., 1999; Jiang & Wise, 2009; Röhl et al., 2000, 2007; Zachos et al., 2005).

4.4. Misguided Paleoecological Inferences

The stable isotope signatures of acarininids and subbotinids indicate that the paleoecologies of these two genera differed. Acarininid shells consistently return lower $\delta^{18}O$ and higher $\delta^{13}C$ values than those registered by contemporaneous subbotinid shells (e.g., Berggren & Norris, 1997; Corfield & Cartlidge, 1991; Quillévéré & Norris, 2003; Shackleton et al., 1985). In addition, the $\delta^{13}C$ signatures of acarininid species conform to a size-dependent trend that is similar to the positive $\delta^{13}C$-size covariation seen in modern planktic foraminifers that host algal photosymbionts, whereas $\delta^{13}C$-size covariation is negligible in the subbotinids (D'Hondt et al., 1994; Norris, 1996). These differences in stable isotope signatures indicate that the acarininids likely harbored photosymbionts and inhabited the warm, sunlit waters of the oceanic mixed layer, while the asymbiotic subbotinids inhabited deeper, cooler waters within the thermocline (D'Hondt et al., 1994; Norris, 1996; Quillévéré et al., 2001; Quillévéré & Norris, 2003).

The $\delta^{13}C$-size signal of photosymbiosis is evident in pre-CIE samples of the *A. subsphaerica* and *A. soldadoensis* records (Figures 4a and 4g) but disappears as successively smaller size classes register CIE values up through the Site 690 PETM section (Figures 4a–4e and 4g–4k). A similar breakdown in the $\delta^{13}C$-size relation of acarininids has been reported in the PETM section of nearby Site 689 (Maud Rise), where it was attributed to the loss of photosymbiosis in response to ocean warming (Si & Aubry, 2018). Photosymbiosis is commonplace among modern planktic foraminifers (Hemleben et al., 1989), so invoking symbiont "bleaching" for the temporary disappearance of its $\delta^{13}C$-size signature in acarininids seems plausible. However, the $\delta^{13}C_{bulk}$ record of the Site 689 PETM section features an attenuated, stepwise CIE much like that at Site 690, and there is sedimentological evidence to indicate that the CIE interval of the Site 689 PETM section has been strongly distorted by sediment mixing (Kelly et al., 2012). In addition, symbiont bleaching in response to thermal stress would most likely occur in the tropics, yet size-segregated $\delta^{13}C$ records show that tropical planktic foraminifers retained the $\delta^{13}C$-size signature of photosymbiosis during the PETM (Kelly et al., 1998). Thus, there is ample evidence, albeit somewhat circumstantial, to indicate that the disappearance of the $\delta^{13}C$-size relation in acarininids may be yet another taphonomic artifact of SDSM. Here we revisit this issue and present evidence further implicating SDSM as the cause for the transient disappearance of $\delta^{13}C$-size covariation in acarininids at Site 690.

If symbiont bleaching occurred during the PETM, one would expect to see an immediate response where all size fractions simultaneously record CIE values and a $\delta^{13}C$-size relation with a negligible slope, as shown by culturing studies (Spero & Lea, 1993). Instead, our time series of size-segregated acarininid records show that the $\delta^{13}C$ values of larger shells (>250 μm) abruptly decrease by ~4‰, while smaller shells of *A. subsphaerica* and *A. soldadoensis* continue to show pre-CIE values (see Figures 5b–5c and 5h–5i). This size-dependent pattern of isotopic change is consistent with SDSM, where smaller shells are preferentially displaced up-section relative to larger shells. Even the "transitional" $\delta^{13}C$ values returned by the smaller size classes are readily explained by SDSM because these pooled, multishell samples are likely mixtures of varying proportions of pre-CIE and CIE specimens (Hupp et al., 2019).

A similar sequential pattern of size-dependent change is seen in the $\delta^{13}C$-size relation of the subbotinids (Figures 4m–4q). The finding that larger (>212 μm) shells record CIE values before smaller shells among the subbotinids (Figure 4o) is of interest because this genus is considered to have been asymbiotic owing to its negligible $\delta^{13}C$-size relation (Figure 4m). Yet the sequential manner in which the $\delta^{13}C$-size relation of asymbiotic subbotinids changes (Figures 4m–4q) is similar to that seen in the symbiotic acarininids. Thus, the size-dependent manner in which the $\delta^{13}C$-size relation changes in the subbotinids contradicts the view that acarininids expelled their photosymbionts during the PETM and instead points to SDSM as a common cause.

The δ^{13}C-size relations of all three taxa change in a similar sequential manner, but the relative timing and apparent rate of this change differ between the taxa. All size fractions of *A. soldadoensis* complete the transition to CIE values by ~12 cm above the stratigraphic level of the bulk CIE onset (Figure 4j), whereas the various size classes of *A. subsphaerica* do not fully transition to CIE values until ~47 cm above the same datum (Figure 4e). Furthermore, the transition to CIE values among the subbotinid size fractions occurs over a much shorter stratigraphic interval than in the acarininids and first initiates ~9 cm above where it initiates in the acarininid δ^{13}C-size records (Figures 4o and 4p). Mixing models indicate that such disparities in the timing and rate of size-dependent isotopic change may be related to differences in the relative abundances of the three taxa (Kirtland Turner et al., 2017). For example, *A. subsphaerica* is more abundant than *A. soldadoensis* within the pre-CIE interval, whereas the opposite is true for the overlying CIE interval at Site 690 (Kelly, 2002). Hence, the probability of encountering a reworked pre-CIE shell within the CIE interval is higher for *A. subsphaerica* than *A. soldadoensis*, and the greater proportion of pre-CIE *A. subsphaerica* shells in conjunction with SDSM would have the net effect of displacing the CIE onset further up-section among the smaller shells of this species. We suspect that the same principle applies to the subbotinids, as their relative abundance decreases markedly across the bulk CIE onset (Kelly, 2002). Further, the subbotinid time series was constructed at the genus level, so it does not capture the stratigraphic details seen in the species-level records constructed for the acarininids.

Planktic foraminifer communities responded to PETM warming through extratropical migrations, resulting in the arrival of warm-water, immigrant taxa at high-latitude sites (Kelly, 2002; Lu & Keller, 1993). This restructuring of planktic foraminifer biogeographic distributions is exemplified by the first appearance of species belonging to the genus *Morozovella* spp. within the CIE intervals of high-latitude Sites 689 and 690 (Kelly et al., 2012). The first appearance of morozovellids at Sites 689 and 690 is relevant because the stable isotope compositions of morozovellid shells are very similar to those of acarininids (Norris, 1996), and it has been shown that the distinctive δ^{13}C-size signature of photosymbiosis is maintained by morozovellids while it disappears among the acarininids through the CIE interval of Site 689 (Si & Aubry, 2018). We posit that this intergeneric discrepancy is also due to differences between the relative abundances of acarininids and morozovellids in the Site 689 PETM section. Unlike the acarininids, morozovellid populations did not exist in the Weddell Sea region prior to the CIE onset (Kelly, 2002; Kelly et al., 2012), so all morozovellid size fractions are composed solely of CIE shells. As a consequence, the positive δ^{13}C-size relation signaling photosymbiosis is conserved in the morozovellids.

The series of δ^{18}O-size records constructed for the acarininids show a sequential pattern of size-dependent change that is nearly identical to that seen in complementary δ^{13}C-size records. The two largest size classes of *A. subsphaerica* first register CIE and OIE values at −6 cm, while smaller size classes of the same sample continue to return pre-CIE and pre-OIE values (Figures 4b and 5b). In the succeeding sample (+3 cm), shells from the three largest size class of *A. subsphaerica* return CIE/OIE values, while the 212–250 μm size fraction registers transitional δ^{13}C and δ^{18}O values and the two smallest size fractions (<212 μm) continue to show pre-CIE and pre-OIE values (Figures 4c and 5c). Thus, a sequential pattern of size-dependent change progresses up through the series of δ^{18}O-size records much as it does in the series of δ^{13}C-size records until all *A. subsphaerica* size classes eventually register OIE values at +47 cm (Figures 5a–5e).

Likewise, a high degree of similitude exists between the parallel δ^{13}C- and δ^{18}O-size records generated for *A. soldadoensis* (Figures 4h–4k and 5g–5j) and the subbotinids (Figures 4n–4r and 5l–5q). However, a direct comparison of the subbotinid δ^{18}O- and δ^{13}C-size records reveals a couple of minor irregularities between these two complementary records. The first involves the sample at −6 cm, where the δ^{13}C ratio recorded by the largest subbotinid size fraction (300–355 μm) is clearly a pre-CIE value (Figure 4n), yet the same subbotinid size fraction (300–355 μm) registers a δ^{18}O ratio approaching an OIE value (Figure 5m). This apparent inconsistency is also evident in the single-shell stable isotope records published for the Site 690 PETM section (Figures 2b and 2c) and may reflect ocean warming prior to carbon input as previously reported (Thomas et al., 2002). The other minor departure from the overall stratigraphic pattern of δ^{18}O-size variation occurs at 0 cm, where the largest subbotinid size fraction (300–355 μm) registers a δ^{18}O value that is slightly higher than those of the smaller size fractions (Figures 5n).

We consider the minor vagaries of the subbotinid δ^{18}O-size records immaterial since there is no δ^{18}O-size signature indicative of photosymbiosis (D'Hondt et al., 1994; Norris, 1996; Spero & Lea, 1993), yet the series of δ^{18}O-size records constructed for the symbiotic acarininids reproduce all salient aspects of the complementary δ^{13}C-size records. Moreover, the interspecies differences in timing/rate at which the δ^{13}C values of various size classes record CIE values are closely tracked by the δ^{18}O-size records of all three taxa (Figure 5). The congruency between the δ^{13}C- and δ^{18}O-size records of the symbiotic acarininids and asymbiotic subbotinids is incompatible with a paleoecological explanation involving the loss of photosymbiosis.

The apparent "flattening" of the δ^{13}C-size slope delineated by *A. subsphaerica* shells at + 47 cm (Figure 4e) and *A. soldadoensis* shells over the interval spanning + 12 to + 47 cm (Figures 4j–4k) may seem consistent with the loss of photosymbiosis, but it should be kept in mind that the δ^{13}C-size (Figures 4a–4e and 4g–4i) and δ^{18}O-size (Figures 5a–5e and 5g–5h) records of these same species clearly show that SDSM caused the disappearance of positive δ^{13}C-size covariation to begin with. It therefore stands to reason that the pooled, multishell analyses used to measure the δ^{13}C of the smaller size fractions likely contain pre-CIE shells with higher δ^{13}C values. This supposition is supported by the sediment-mixing curves indicating that this part of the CIE interval (~170.51–170.16 mbsf) still contains minor amounts of fine-fraction carbonate from the underlying pre-CIE interval (Figure 6). The presence of even a few pre-CIE shells would elevate the δ^{13}C values of the smaller size classes relative to those of the larger size classes, thereby flattening the slope of the δ^{13}C-size relation over this part of the stratigraphy.

The δ^{13}C values of larger (>250 μm) acarininid shells increase by ~1–2‰ in the uppermost sample (+62 cm) of the study section, resulting in the reappearance of positive δ^{13}C-size covariation among the acarininids (Figures 4f and 4l). The restoration of this positive δ^{13}C-size relation could be construed as signaling the reacquisition of photosymbionts by acarininids; however, the δ^{13}C increase registered by large (>250 μm) acarininid shells coincides with the CIE minimum in the $\delta^{13}C_{bulk}$ record (Figures 2a and 2b). Thus, δ^{13}C values of large acarininid shells begin to recover to higher values over the same interval where nannofossil-dominated $\delta^{13}C_{bulk}$ values continue to decline. These antithetic δ^{13}C trends are readily reconciled by SDSM; only at this point in the stratigraphy is fine-fraction carbonate from the CIE interval being mixed upward into the overlying CIE "recovery" interval. The blending of smaller CIE shells with anomalously low δ^{13}C values and larger recovery shells with higher δ^{13}C values would enhance positive δ^{13}C-size covariation among the acarininids as is seen in the uppermost sample (+62 cm) of our study section (Figures 4f and 4l). Moreover, published records (Kennett & Stott, 1991) show that the δ^{13}C values of asymbiotic subbotinids also increase ~50 cm (~169.75 mbsf) above the stratigraphic level where acarininid δ^{13}C values begin to increase. Thus, both asymbiotic subbotinids and symbiotic acarininids show a similar δ^{13}C increase, which further contradicts the view that the reestablishment of photosymbiosis caused the δ^{13}C increase in acarininids during the earliest stage of the CIE recovery at Site 690.

Finally, the δ^{13}C increase registered by large (>250 μm) acarininid shells at ~170.26 mbsf is accompanied by a secondary ~1‰ decrease in corresponding δ^{18}O values (Figures 2b and 2c). Paired δ^{18}O:Mg/Ca ratio measurements have shown that this secondary decrease in acarininid δ^{18}O values reflects a significant decrease in surface-ocean δ^{18}O composition at Site 690 (Kozdon et al., 2020). Yet only large shells (300–355 μm) of *A. subsphaerica* clearly record this decrease in surface-ocean δ^{18}O composition at + 62 cm, while shells from the two smallest size fractions (150–180 μm and 180–212 μm) continue to show higher δ^{18}O values centered on −1‰ (Figure 5f). A similar size-dependent pattern of isotopic change is expressed in the δ^{18}O-size relation of *A. soldadoensis* at + 62 cm (Figure 5k), although smaller shells in some of the preceding samples return unusually low δ^{18}O values (Figures 5i and 5j). Apart from the minor inconsistencies noted in the *A. soldadoensis* δ^{18}O-size records, the δ^{18}O-size relations of the acarininid species at + 62 cm (Figures 5f and 5k) also implicate SDSM as a causal factor in the initial reappearance of positive δ^{13}C-size covariation. This being said, we close by noting that the identifiable effects of SDSM will dissipate as one moves into parts of the Site 690 record that lie beyond the stratigraphic scope of isotopic change associated with the PETM or other intervals of abrupt isotopic change. Thus, the reappearance of the δ^{13}C-size signature of photosymbiosis is an expected outcome consonant with the SDSM model herein proposed.

5. Conclusions

Stable isotope (δ^{13}C and δ^{18}O) records constructed with graduated series of size-segregated shells of three planktic foraminifer taxa (*A. subsphaerica*, *A. soldadoensis*, and *Subbotina* spp.) show that stratigraphic positions of the onsets of both the CIE and OIE are dependent upon shell size in the Site 690 PETM section. The sequential manner in which each successive sample leads to the next smallest size fraction registering CIE/OIE values up through the Site 690 PETM section is best explained by SDSM, where finer-sized materials are more intensely mixed and preferentially displaced up-section relative to coarser-sized materials. The size-dependent patterns of isotopic change indicate that taphonomic processes such as size-selective feeding by infauna (i.e., bioturbation) and/or bottom-water currents have winnowed the sedimentary record of the CIE interval. As a result, the use of relatively large (>250 μm) foraminifer shells to construct high-resolution records of the CIE/OIE is encouraged, as larger shells are less susceptible to upward displacement in pelagic sedimentary records.

SDSM gives rise to phase lags between parallel isotope stratigraphies constructed with differing foraminifer size fractions, where the records of smaller shells are shifted up-section relative to those of larger shells. The sense and direction of these size-dependent phase lags suggest that the $\delta^{13}C_{bulk}$ and $\delta^{18}O_{bulk}$ records, which primarily reflect the isotopic composition of fine-fraction nannofossil carbonate, have also been shifted up-section. This inference accounts for the stratigraphic offset in the CIE/OIE onset between the records of nannofossil-dominated bulk-carbonate and large shells of shallow-dwelling acarininids. Moreover, the time-averaging effects of SDSM have clearly smoothed and attenuated the isotopic excursions in the nannofossil-dominated bulk-carbonate records. The combined effects of preferential upward displacement and smoothing of isotopic excursions also result in transitory inversions of isotope gradients between the records of bulk-carbonate and larger foraminifer shells.

Deterministic, two end-member mixing curves suggest that the stepped structure of the bulk CIE record is a taphonomic signal of varying proportions of pre-CIE material reworked up through the overlying CIE interval. The series of fine-scale decreases (steps) in the $\delta^{13}C_{bulk}$ record reflect minor jumps in the accumulation rates of CIE carbonate, which dilute the amount of pre-CIE contamination and cause $\delta^{13}C_{bulk}$ values to decrease in an intermittent fashion. The series of upticks in CIE carbonate accumulation rates are related to progressive, but discontinuous, redeepening of the carbonate lysocline following its initial shoaling in response to carbon input at the CIE onset. The stepped CIE structure in $\delta^{13}C_{bulk}$ records of other pelagic PETM sections attests to the pervasive nature of SDSM in pelagic sediments and indicates that the history of lysocline redeepening may have been more complex than presently perceived. This being said, the fine-scale steps in $\delta^{13}C_{bulk}$ are still considered reliable datums for intersite chemostratigraphic correlation over broad geographic regions, mostly in the Atlantic Ocean basin.

The stratigraphic series of size-segregated $\delta^{13}C$ and $\delta^{18}O$ records also show that SDSM temporarily masks $\delta^{13}C$-size covariation among planktic foraminifers within the CIE interval of the Site 690 section. The $\delta^{13}C$-size and $\delta^{18}O$-size records of both symbiotic acarininids and asymbiotic subbotininds show similar sequential, size-dependent patterns of change. Thus, the transitory loss of this size-dependent $\delta^{13}C$ signal is not a paleoecological signal of symbiont "bleaching" during the PETM.

The rich data set herein reported has far-reaching implications for pelagic sedimentary records of the PETM and other paleoclimate events marked by abrupt changes in geochemistry. Cursory examination of the published literature reveals that size-dependent phase lags and shifts similar to those found in this study occur in the stable isotope stratigraphies and geochronologies constructed for deep-sea records of Quaternary climate change (e.g., Ohkouchi et al., 2002; Paull et al., 1991). This realization indicates that SDSM pervades the pelagic sedimentary record, and failure to recognize its taphonomic signature can lead to erroneous interpretations.

Acknowledgments
Funding for this work was provided by student grants to B.H. from the American Association of Petroleum Geologists (AAPG), Geological Society of America (GSA), and Society for Sedimentary Geology (SEPM). Thanks to Colin Carney and Dyke Andreason for technical support and Ariel Jaeger for laboratory assistance. We thank editor Ursula Röhl, Dustin Harper, and two anonymous reviewers for their insightful comments, which improved our manuscript.

Data Availability Statement

Carbon and oxygen isotope data can be accessed via the NOAA Paleoclimatology Database at https://www.ncdc.noaa.gov/paleo-search/study/30852.

References

Ajayi, S., Kump, L. R., Ridgwell, A., Kirtland Turner, S., Hay, C. C., & Bralower, T. J. (2020). Evaluation of Paleocene-Eocene Thermal Maximum carbon isotope record completeness—An illustration of the potential of dynamic time warping in aligning paleo-proxy records. *Geochemistry, Geophysics, Geosystems*, *21*, e2019GC008620. https://doi.org/10.1029/2019GC008620

Aubry, M. P., Ouda, K., Dupuis, C., Berggren, W. A., Van Couvering, J. A., & the Members of the Working Group on the Paleocene/Eocene Boundary (2007). The Global Standard Stratotype-section and Point (GSSP) for the base of the Eocene Series in the Dababiya section (Egypt). *Episodes*, *30*(4), 271–286. https://doi.org/10.18814/epiiugs/2007/v30i4/003

Aze, T., Pearson, P. N., Dickson, A. J., Badger, M. P. S., Bown, P. R., Pancost, R. D., et al. (2014). Extreme warming of tropical waters during the Paleocene-Eocene Thermal Maximum. *Geology*, *42*(9), 739–742. https://doi.org/10.1130/G35637.1

Babila, T. L., Penman, D. E., Hönisch, B., Clay Kelly, D., Bralower, T. J., Rosenthal, Y., & Zachos, J. C. (2018). Capturing the global signature of surface ocean acidification during the Palaeocene-Eocene Thermal Maximum. *Philosophical Transactions of the Royal Society A: Mathematical, Physical and Engineering Sciences*, *376*(2130). https://doi.org/10.1098/rsta.2017.0072

Bains, S., Corfield, R. M., & Norris, R. D. (1999). Mechanisms of climate warming at the end of the Paleocene. *Science*, *285*(5428), 724–727. https://doi.org/10.1126/science.285.5428.724

Bard, E. (2001). Paleoceanographic implications of the difference in deep-sea sediment mixing between large and fine particles. *Paleoceanography*, *16*(3), 235–239. https://doi.org/10.1029/2000PA000537

Barker, P. E., Kennett, J. P., O'Connell, S., Berkowitz, S., Bryant, W. R., Burkle, L. H., et al. (1988). *Proceedings of the Ocean Drilling Program, Initial Reports, 113*. College Station, TX: Ocean Drilling Program. https://doi.org/10.2973/odp.proc.ir.113.1988

Berger, W. H., & Heath, G. R. (1968). Vertical mixing in pelagic sediments. *Journal of Marine Research*, *26*(2), 134–143.

Berger, W. H., & Johnson, R. F. (1978). On the thickness and the ^{14}C age of the mixed layer in deep-sea carbonates. *Earth and Planetary Science Letters*, *41*, 223–227. https://doi.org/10.1016/0012-821X(78)90012-2

Berggren, W. A., & Norris, R. D. (1997). Biostratigraphy, phylogeny and systematics of Paleocene trochospiral planktic foraminifera. *Micropaleontology*, *43*, 1–116. https://doi.org/10.2307/1485988

Bowen, G. J., & Bowen, B. B. (2008). Mechanisms of PETM global change constrained by a new record from central Utah. *Geology*, *36*(5), 379–382. https://doi.org/10.1130/G24597A.1

Bowen, G. J., Maibauer, B. J., Kraus, M. J., Röhl, U., Westerhold, T., Steimke, A., et al. (2015). Two massive, rapid releases of carbon during the onset of the Palaeocene-Eocene Thermal Maximum. *Nature Geoscience*, *8*, 44–47. https://doi.org/10.1038/ngeo2316

Bralower, T. J. (2002). Evidence of surface water oligotrophy during the Paleocene-Eocene Thermal Maximum, nannofossil assemblage data from Ocean Drilling Program Site 690, Maud Rise, Weddell Sea. *Paleoceanography*, *17*(2), 9. https://doi.org/10.1029/2001PA000662

Bralower, T. J., Kelly, D. C., Gibbs, S., Farley, K., Eccles, L., Lindemann, T. L., & Smith, G. J. (2014). Impact of dissolution on the sedimentary record of the Paleocene-Eocene Thermal Maximum. *Earth and Planetary Science Letters*, *401*, 70–82. https://doi.org/10.1016/j.epsl.2014.05.055

Corfield, R. M., & Cartlidge, J. E. (1991). Isotopic evidence for the depth stratification of fossil and recent Globigerinina: A review. *Historical Biology*, *5*(1), 37–63. https://doi.org/10.1080/10292389109380387

D'Hondt, S., Zachos, J. C., & Schultz, G. (1994). Stable isotopic signals and photosymbiosis in Late Paleocene planktic foraminifera. *Paleobiology*, *20*, 391–406. https://doi.org/10.1017/s0094837300012847

Dickens, G. R., Castillo, M. M., & Walker, J. C. G. (1997). A blast of gas in the latest Paleocene: Simulating first-order effects of massive dissociation of oceanic methane hydrate. *Geology*, *25*(3), 259–262. https://doi.org/10.1130/0091-7613(1997)025<0259:ABOGIT>2.3.CO;2

Dickens, G. R., O'Neil, J. R., Rea, D. K., & Owen, R. M. (1995). Dissociation of oceanic methane hydrate as a cause of the carbon isotope excursion at the end of the Paleocene. *Paleoceanography*, *10*(6), 965–971. https://doi.org/10.1029/95PA02087

Dunkley Jones, T., Lunt, D. J., Schmidt, D. N., Ridgwell, A., Sluijs, A., Valdes, P. J., & Maslin, M. (2013). Climate model and proxy data constraints on ocean warming across the Paleocene-Eocene Thermal Maximum. *Earth-Science Reviews*, *125*, 123–145. https://doi.org/10.1016/j.earscirev.2013.07.004

Edgar, K. M., Anagnostou, E., Pearson, P. N., & Foster, G. L. (2015). Assessing the impact of diagenesis on δ^{11}B, δ^{13}C, δ^{18}O, Sr/Ca and B/Ca values in fossil planktic foraminiferal calcite. *Geochimica et Cosmochimica Acta*, *166*, 189–209. https://doi.org/10.1016/j.gca.2015.06.018

Farley, K. A., & Eltgroth, S. F. (2003). An alternative age model for the Paleocene-Eocene Thermal Maximum using extraterrestrial 3H. *Earth and Planetary Science Letters*, *208*(135), 148. https://doi.org/10.1016/S0012-821X(03)00017-7

Glass, B. P. (1969). Reworking of deep-sea sediments as indicated by the vertical dispersion of the Australasian and Ivory Coast microtektite horizons. *Earth and Planetary Science Letters*, *6*, 409–415. https://doi.org/10.1016/0012-821X(69)90109-5

Hemleben, C., Spindler, M., & Anderson, O. R. (1989). Host and symbiont relationships. In *Modern planktonic foraminifera* (86–111). New York, NY: Springer. https://doi.org/10.1007/978-1-4612-3544-6_5

Hupp, B. N., Kelly, D. C., Zachos, J. C., & Bralower, T. J. (2019). Effects of size-dependent sediment mixing on deep-sea records of the Paleocene-Eocene Thermal Maximum. *Geology*, *47*(8), 749–752. https://doi.org/10.1130/G46042.1

Jiang, S., & Wise, S. W. Jr. (2009). Distinguishing the influence of diagenesis on the paleoecological reconstruction of nannoplankton across the Paleocene/Eocene Thermal Maximum: An example from the Kerguelen Plateau, southern Indian Ocean. *Marine Micropaleontology*, *72*, 49–59. https://doi.org/10.1016/j.marmicro.2009.03.003

Jumars, P. A., Nowell, A. R. M., & Self, F. L. (1981). A simple model of flow-sediment-organism interaction. *Marine Geology*, *42*, 155–172. https://doi.org/10.1016/S0070-4571(08)70298-X

Kelly, D. C. (2002). Response of Antarctic (ODP Site 690) planktonic foraminifera to the Paleocene-Eocene Thermal Maximum: Faunal evidence for ocean/climate change. *Paleoceanography*, *17*(4), 1–13. https://doi.org/10.1029/2002PA000761

Kelly, D. C., Bralower, T. J., & Zachos, J. C. (1998). Evolutionary consequences of the latest Paleocene Thermal Maximum for tropical planktonic foraminifera. *Palaeogeography, Palaeoclimatology, Palaeoecology*, *141*(1–2), 139–161. https://doi.org/10.1016/S0031-0182(98)00017-0

Kelly, D. C., Nielsen, T. M. J., McCarren, H. K., Zachos, J. C., & Röhl, U. (2010). Spatiotemporal patterns of carbonate sedimentation in the South Atlantic: Implications for carbon cycling during the Paleocene-Eocene Thermal Maximum. *Palaeogeography, Palaeoclimatology, Palaeoecology*, *293*(1–2), 30–40. https://doi.org/10.1016/j.palaeo.2010.04.027

Kelly, D. C., Nielsen, T. M. J., & Schellenberg, S. A. (2012). Carbonate saturation dynamics during the Paleocene-Eocene Thermal Maximum: Bathyal constraints from ODP Sites 689 and 690 in the Weddell Sea (South Atlantic). *Marine Geology*, *303–306*, 75–86. https://doi.org/10.1016/j.margeo.2012.02.003

Kelly, D. C., Zachos, J. C., Bralower, T. J., & Schellenberg, S. A. (2005). Enhanced terrestrial weathering/runoff and surface ocean carbonate production during the recovery stages of the Paleocene-Eocene Thermal Maximum. *Paleoceanography*, *20*, 11. https://doi.org/10.1029/2005PA001163

Kennett, J. P., & Stott, L. D. (1991). Abrupt deep-sea warming, paleoceanographic changes and benthic extinctions at the end of the Palaeocene. *Nature*, *353*, 225–229. https://doi.org/10.1038/353225a0

Kirtland Turner, S., Hull, P. M., Kump, L. R., & Ridgwell, A. (2017). A probabilistic assessment of the rapidity of PETM onset. *Nature Communications*, *8*(353), 1–10. https://doi.org/10.1038/s41467-017-00292-2

Koch, P. L., Zachos, J. C., & Gingerich, P. D. (1992). Correlation between isotope records in marine and continental carbon reservoirs near the Palaeocene/Eocene boundary. *Nature*, *358*(6384), 319–322. https://doi.org/10.1038/358319a0

Kozdon, R., Kelly, D. C., Kitajima, K., Strickland, A., Fournelle, J. H., & Valley, J. W. (2013). In situ δ^{18}O and Mg/Ca analyses of diagenetic and planktic foraminiferal calcite preserved in a deep-sea record of the Paleocene-Eocene Thermal Maximum. *Paleoceanography*, *28*, 517–528. https://doi.org/10.1002/palo.20048

Kozdon, R., Penman, D. E., Kelly, D. C., Zachos, J. C., Fournelle, J. H., & Valley, J. W. (2020). Enhanced poleward flux of atmospheric moisture to the Weddell Sea Region (ODP Site 690) during the Paleocene-Eocene Thermal Maximum. *Paleoceanography and Paleoclimatology*, *35*. https://doi.org/10.1029/2019PA003811

Lu, G., & Keller, G. (1993). The Paleocene-Eocene transition in the Antarctic Indian Ocean: Inference from planktic foraminifera. *Marine Micropaleontology*, *21*, 101–142. https://doi.org/10.1016/0377-8398(93)90012-m

McInerney, F. A., & Wing, S. L. (2011). The Paleocene-Eocene Thermal Maximum: A perturbation of carbon cycle, climate, and biosphere with implications for the future. *Annual Review of Earth and Planetary Sciences*, *39*, 489–516. https://doi.org/10.1146/annurev-earth-040610-133431

Murray, J. M. H., Meadows, A., & Meadows, P. S. (2002). Biogeomorphological implications of microscale interactions between sediment geotechnics and marine benthos: A review. *Geomorphology*, *47*(1), 15–30. https://doi.org/10.1016/S0169-555X(02)00138-1

Norris, R. D. (1996). Symbiosis as an evolutionary innovation in the radiation of Paleocene planktic foraminifera. *Paleobiology*, *22*(4), 461–480. https://doi.org/10.1017/S0094837300016468

Ohkouchi, N., Eglinton, T. I., Keigwin, L. D., & Hayes, J. M. (2002). Spatial and temporal offsets between proxy records in a sediment drift. *Science*, *298*(5596), 1224–1227. https://doi.org/10.1126/science.1075287

Paull, C. K., Hills, S. J., Thierstein, H. R., Bonani, G., & Wölfli, W. (1991). ^{14}C offsets and apparently non-synchronous δ^{18}O stratigraphies between nannofossil and foraminiferal pelagic carbonates. *Quaternary Research*, *35*(2), 274–290. https://doi.org/10.1016/0033-5894(91)90073-E

Pearson, P. N., Ditchfield, P. W., Singano, J., Harcourt-Brown, K. G., Nicholas, C. J., Olsson, R. K., et al. (2001). Warm tropical sea surface temperatures in the Late Cretaceous and Eocene epochs. *Nature*, *413*(6855), 481–487. https://doi.org/10.1038/35097000

Peng, T. H., Broecker, W. S., & Berger, W. H. (1979). Rates of benthic mixing in deep-sea sediment as determined by radioactive tracers. *Quaternary Research*, *11*, 141–149.

Penman, D. E., Turner, S. K., Sexton, P. F., Norris, R. D., Dickson, A. J., Boulila, S., et al. (2016). An abyssal carbonate compensation depth overshoot in the aftermath of the Palaeocene-Eocene Thermal Maximum. *Nature Geoscience*, *9*(8), 575–580. https://doi.org/10.1038/ngeo2757

Penman, D. E., & Zachos, J. C. (2018). New constraints on massive carbon release and recovery processes during the Paleocene-Eocene Thermal Maximum. *Environmental Research Letters*, *13*(10). https://doi.org/10.1088/1748-9326/aae285

Quillévéré, F., & Norris, R. D. (2003). Ecological development of acarininids (planktonic foraminifera) and hydrographic evolution of Paleocene surface waters. *Special Paper of the Geological Society of America*, *369*(May 2014), 223–238. https://doi.org/10.1130/0-8137-2369-8.223

Quillévéré, F., Norris, R. D., Moussa, I., & Berggren, W. A. (2001). Role of photosymbiosis and biogeography in the diversification of early Paleogene acarininids (planktonic foraminifera). *Paleobiology*, *21*(2), 311–326. https://doi.org/10.1666/0094-8373(2001)027<0311:ROPABI>2.0.CO;2

Ridgwell, A. (2007). Interpreting transient carbonate compensation depth changes by marine sediment core modeling. *Paleoceanography*, *22*, 1–10. https://doi.org/10.1029/2006PA001372

Röhl, U., Bralower, T. J., Norris, R. D., & Wefer, G. (2000). New chronology for the late Paleocene thermal maximum and its environmental implications. *Geology*, *28*(10), 927–930. https://doi.org/10.1130/0091-7613(2000)28<927:NCFTLP>2.0.CO;2

Röhl, U., Westerhold, T., Bralower, T. J., & Zachos, J. C. (2007). On the duration of the Paleocene-Eocene Thermal Maximum (PETM). *Geochemistry, Geophysics Geosystems*, *8*, Q12002. https://doi.org/10.1029/2007GC001784

Schiffelbein, P. (1984). Effect of benthic mixing on the information content of deep-sea stratigraphic signals. *Nature*, *311*, 651–653. https://doi.org/10.1038/311651a0

Seibold, E. (1978). Mechanical processes influencing the distribution of pelagic sediments. *Micropaleontology*, *24*(4), 407–421. https://doi.org/10.2307/1485370

Shackleton, N. J., Corefield, R. M., & Hall, M. A. (1985). Stable isotope data and the ontogeny of Paleocene planktonic foraminifera. *Journal of Foraminiferal Research*, *15*, 321–336. https://doi.org/10.2113/gsjfr.15.4.321

Si, W., & Aubry, M. P. (2018). Vital effects and ecologic adaptation of photosymbiont-bearing planktonic foraminifera during the Paleocene-Eocene Thermal Maximum, implications for paleoclimate. *Paleoceanography and Paleoclimatology*, *33*(1), 14. https://doi.org/10.1002/2017PA003219

Spero, H. J., & Lea, D. W. (1993). Intraspecific stable isotope variability in the planktic foraminifera *Globigerinoides sacculifer*: Results from laboratory experiments. *Marine Micropaleontology*, *22*, 221–234. https://doi.org/10.1016/0377-8398(93)90045-Y

Stainbank, S., Spezzaferri, S., De Boever, E., Bouvier, A. S., Chilcott, C., de Leau, E. S., et al. (2020). Assessing the impact of diagenesis on foraminiferal geochemistry from a low latitude, shallow-water drift deposit. *Earth and Planetary Science Letters*, *545*(116390). https://doi.org/10.1016/j.epsl.2020.116390

Stoll, H. M. (2005). Limited range of interspecific vital effects in coccolith stable isotopic records during the Paleocene-Eocene Thermal Maximum. *Paleoceanography*, *20*, 10. https://doi.org/10.1029/2004PA001046

Svenson, H., Planke, S., Maithe-Sørensen, A., Jamtveit, B., Myklebust, R., Eidem, T. R., & Rey, S. S. (2004). Release of methane from a volcanic basin as a mechanism for initial Eocene global warming. *Nature*, *429*(6991), 542–545. https://doi.org/10.1038/nature02566

Taghon, G. L. (1982). Optimal foraging by deposit-feeding invertebrates: Roles of particle size and organic coating. *Oecologia*, *52*, 295–304. https://doi.org/10.1007/BF00367951

Thomas, D. J., Zachos, J. C., Bralower, T. J., Thomas, E., & Bohaty, S. (2002). Warming the fuel for the fire: Evidence for the thermal dissociation of methane hydrate during the Paleocene-Eocene Thermal Maximum. *Geology*, *30*(12), 1067–1070. https://doi.org/10.1130/0091-7613(2002)030<1067:WTFFTF>2.0.CO;2

Thomas, E. (1990). Late Cretaceous through Neogene deep-Sea benthic foraminifers (Maud Rise, Weddell Sea, Antarctica). In P. F. Barker, J. P. Kennett, et al. (Eds.), *Proceedings of the Ocean Drilling Program, Scientific Results, 113* (pp. 571–594). College Station, TX: Ocean Drilling Program.

Westerhold, T., Röhl, U., Wilkens, R. H., Gingerich, P. D., Clyde, W. C., Wing, S. L., et al. (2018). Synchronizing early Eocene deep-sea and continental records- cyclostratigraphic age models for the Bighorn Basin Coring Project drill cores. *Climate of the Past*, *14*, 303–319. https://doi.org/10.5194/cp-14-303-2018

Wheatcroft, R. A., & Jumars, P. A. (1987). Statistical re-analysis for size dependency in deep sea mixing. *Marine Geology*, *77*, 157–163. https://doi.org/10.1016/0025-3227(87)90090-9

Zachos, J. C., Bohaty, S. M., John, C. M., McCarren, H., Kelly, D. C., & Nielsen, T. (2007). The Palaeocene-Eocene carbon isotope excursion: Constraints from individual shell planktonic foraminifer records. *Philosophical Transactions of the Royal Society A: Mathematical, Physical and Engineering Sciences*, *365*(1856), 1829–1842. https://doi.org/10.1098/rsta.2007.2045

Zachos, J. C., Röhl, U., Schellenberg, S. A., Sluijs, A., Hodell, D. A., Kelly, D. C., et al. (2005). Rapid acidification of the ocean during the Paleocene-Eocene Thermal Maximum. *Science*, *308*(5728), 1611–1615. https://doi.org/10.1126/science.1109004

Zeebe, R. E., Zachos, J. C., & Dickens, G. R. (2009). Carbon dioxide forcing alone insufficient to explain Palaeocene-Eocene Thermal Maximum warming. *Nature Geoscience*, *2*(8), 576–580. https://doi.org/10.1038/ngeo578

Zhang, Q., Ding, L., Kitajima, K., Valley, J. W., Zhang, B., Xu, X., et al. (2020). Constraining the magnitude of the carbon isotope excursion during the Paleocene-Eocene Thermal Maximum using larger benthic foraminifera. *Global and Planetary Change*, *184*(103049). https://doi.org/10.1016/j.gloplacha.2019.103049